Electronic Supporting Information (ESI) for

Halide-regulated growth of electrocatalytic metal nanoparticles directly onto a carbon paper electrode

Yaovi Holade,[a] David P. Hickey,[a] and Shelley D. Minteer[a]*.

[a] Departments of Chemistry and Materials Science and Engineering, University of Utah, 315 S 1400 E Rm 2020, Salt Lake City, Utah, 84112, United States.

*Corresponding Author (S.D.M): minteer@chem.utah.edu.

Depending on the concentration, the UV-Vis spectrum of the aqueous solution of $HAuCl_4$ shows one main peak at 200-220 nm accompanied with a shoulder around 290-320 nm (Figure S2d), both attributed to the ligand-to-metal charge transfer transition phenomenon in metal complex ions $[AuCl_4]^-$.[1] Among the relatively stable Au(I) and Au(III) complexes of gold with chloride, Eq. (a1) and (a3) in Table S1 indicates that $[AuCl_2]^-$ acts as "reducing" and "oxidizing" agents. Hence, (a2) is the main equilibrium, as supported by Eq. (1).[2] Table S2 shows that upon the addition of Br^-, $[AuCl_4]^-$ will be completely converted into mixed complexes which evolves towards the more stable $[AuBr_4]^-$ as evidenced by Eq. (2).[3] After the addition of KBr, the main absorption peak at 200-220 nm disappears and two new characteristic features located at 253 and 380 nm can be observed, indicating that $[AuCl_4]^-$ was successfully replaced by $[AuBr_4]^-$ complexes (Figures S2a, S2c, S2e).

$$AuCl_4^-{}_{(aq)} + 2Au_{(s)} + 2Cl^-{}_{(aq)} \rightleftarrows 3AuCl_2^-{}_{(aq)},\ K = 10^{-8} \text{ at } 25\ ^\circ C \quad (1)$$

$$AuBr_4^-{}_{(aq)} + 2Au_{(s)} + 2Br^-{}_{(aq)} \rightleftarrows 3AuBr_2^-{}_{(aq)},\ K = 10^{-6} \text{ at } 25\ ^\circ C \quad (2)$$

Table S1. Standard redox potentials of the involved Au(I) and Au(III) halides.[2,3]

Au(I) and Au(III) species			
Redox couples		Half-cell reaction	E^0 (vs. SHE)
(a1)	$AuCl_2^-/Au$	$AuCl_2^- + e^- \rightleftarrows Au + 2Cl^-$	1.154
(a2)	$AuCl_4^-/Au$	$AuCl_4^- + 3e^- \rightleftarrows Au + 4Cl^-$	1.002
(b1)	$AuBr_2^-/Au$	$AuBr_2^- + e^- \rightleftarrows Au + 2Br^-$	0.959
(a3)	$AuCl_4^-/AuCl_2^-$	$AuCl_4^- + 2e^- \rightleftarrows AuCl_2^- + 2Cl^-$	0.926
(b2)	$AuBr_4^-/Au$	$AuBr_4^- + 3e^- \rightleftarrows Au + 4Br^-$	0.854
(b3)	$AuBr_4^-/AuBr_2^-$	$AuBr_4^- + 2e^- \rightleftarrows AuBr_2^- + 2Br^-$	0.802

Table S2. Dissociation constants of Au(III) halide at 25 °C.[1]

Gold (III) ion-complexes						
-log*Kd*	$[AuCl_4]^-$	$[AuCl_3Br_1]^-$	$[AuCl_2Br_2]^-$	$[AuCl_1Br_3]^-$	$[AuBr_4]^-$	$[AuI_4]^-$
	25	27	29	31	32	48

After the addition of AA, the mixture turns progressively from brown to colorless indicating that Au(III), for instance $[AuBr_4]^-$, is being reduced into the metallic state, i.e., Au^0 by AA (that has a standard redox potential E^0 ≈0.1 V vs. SHE, Scheme S1). The recorded UV-Vis spectrum (Figure S2a) shows that the previous peaks disappear and a new peak at 245 nm appears. The control experiments show that it belongs to the remaining AA (see later in Figure S3d). The colourless solution supported by the absence of any other peaks between 300-1100 nm wavenumber highlight that there is gold nanoparticles in solution and all Au(III) was reduced by AA.

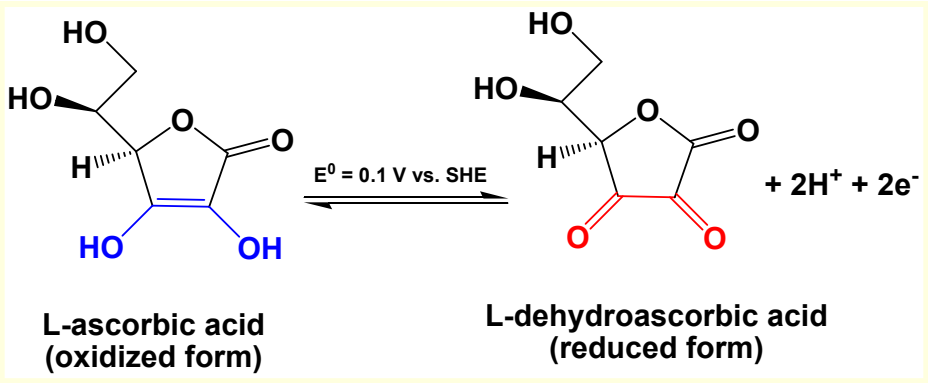

Scheme S1. The use of ascorbic acid as a reduction agent during the chemical reduction reactions.

Table S3. Standard redox potentials of the involved metal complexes with halides.

Redox couples		Half-cell reaction	E^0 (vs. SHE)
Gold	Au^{3+}/Au	$Au^{3+} + 3e^- \rightleftarrows Au$	1.52
	$AuCl_4^-/Au$	$AuCl_4^- + 3e^- \rightleftarrows Au + 4Cl^-$	1.00
	$AuBr_4^-/Au$	$AuBr_4^- + 3e^- \rightleftarrows Au + 4Br^-$	0.85
	AuI_4^-/Au	$AuI_4^- + 3e^- \rightleftarrows Au + 4I^-$	0.56
Platinum	$PtCl_6^{2-}/Pt$	$PtCl_6^{2-} + 4e^- \rightleftarrows Pt + 6Cl^-$	0.76
	$PtBr_6^{2-}/Pt$	$PtBr_6^{2-} + 4e^- \rightleftarrows Pt + 6Br^-$	0.70
Palladium	Pd^{2+}/Pd	$Pd^{2+} + 2e^- \rightleftarrows Pd$	0.91
	$PdCl_4^{2-}/Pd$	$PdCl_4^{2-} + 2e^- \rightleftarrows Pd + 4Cl^-$	0.62
	$PdBr_4^{2-}/Pd$	$PdBr_4^{2-} + 2e^- \rightleftarrows Pd + 4Br^-$	0.49
	PdI_4^{2-}/Pd	$PdI_4^{2-} + 2e^- \rightleftarrows Pd + 4I^-$	0.18

Table S4. Comparison of the production efficiency of gold on 5 cm × 5 cm Toray Carbon Paper TGP-060-H. The metal is deposited on both sides, i.e., a total area of 2 × 25 cm^2 = 50 cm^2. The quantitative analyses were performed by inductively coupled plasma mass spectrometry (ICP-MS).

Samples (reaction time of 30 min at room temperature)	**Theoretical**		**Experimental**		**ICP-MS**
	mg_{metal} cm^{-2}	wt.%	wt.%	Yield (%)[a]	wt.%
Effect of **KBr** amount: $\varphi = n(KBr)/n(HAuCl_4)$					
φ = 0	0.20	4.4	3.3	75	3.0
φ = 2			3.6	82	
φ = 4			3.6	82	
φ = 12			3.6	82	3.4
φ = 24			3.6	82	
φ = 48			3.9	89	
φ = 96			3.8	86	3.6
Halide effect: $\varphi = n(KX)/n(HAuCl_4) = 100$					
KCl	0.40	8.4	4.5	54	4.0
KBr			7.2	86	6.8
KI			7.0	83	5.5
KNO_3			8.2	98	6.5
K_2SO_4			2.5	30	2.0
Effect of **KI** amount: $\varphi = n(KI)/n(HAuCl_4)$					
φ = 4	0.20	4.4	3.3	75	
φ = 12			4.3	98	
φ = 24			3.9	89	
φ = 96			4.1	94	

[a]The yield is defined as "the ratio between the experimental weight and the theoretical one"

Table S5. Comparative performances of relevant direct glucose alkaline fuel cells from literature and those obtained herein: OCV = open circuit voltage; P_{max} = maximum power density, $E_{@Pmax}$ = cell voltage at the maximum power density; "/C" refers to nanoparticles dispersed on carbon black. "RT" refers to room temperature: in our test, this was 20 ± 2 °C.

Design			Performances			Ref.
Cathode (metal loading)	Anode (metal loading)	Fuel (temperature)	OCV (V)	P_{max} (mW cm^{-2})	$E_{@Pmax}$ (V)	
Activated charcoal (2 mg cm^{-2})	60 wt.% PtRu/C (2 mg cm^{-2}): ***commercial***	1 M KOH + 0.2 M glucose (30 °C)	0.90	1.38	0.51	4
		1 M KOH + 0.3 M glucose (30 °C)	0.91	1.08	0.50	
Activated charcoal (3 mg cm^{-2})	40 wt.% Au/C (3 mg cm^{-2})	1 M KOH + 0.3 M glucose (30 °C)	0.85	0.86	0.30	5
	20 wt.% $AuMnO_2$/C (3 mg cm^{-2})		0.86	1.1	0.40	
Activated charcoal (3 mg cm^{-2})	15 wt.% AuPtPd/C (3 mg cm^{-2})	1 M KOH + 0.3 M glucose (30 °C)	0.85	0.52	0.20	6
Activated charcoal (3 mg cm^{-2})	15 wt.% AuPtPd/C (3 mg cm^{-2})	1 M KOH + 0.3 M glucose (30 °C)	0.93	1.0	0.47	7
Pt/C (*unknown*)	Au@carbon paper (3 mg cm^{-2})	0.5 M KOH + 0.3 M glucose (*unknown*)	0.64	0.85	0.31	8
MnO_2/C (0.6 mg cm^{-2})	Mediator methyl viologen	3 M KOH + 1 M glucose (19 °C)	0.53	0.6	0.3	9
		3 M KOH + 1 M glucose (32 °C)	0.55	2.39	0.3	
PtRu nanoparticles (3 mg cm^{-2})	Pt nanoparticles (3 mg cm^{-2})	0.5 M NaOH + 0.5 M glucose (RT)	0.97	20[a]	0.30	10
20 wt.% Pt/C (0.17 mg cm^{-2})	20 wt.% Au/C (0.18 mg cm^{-2})	0.5 M NaOH + 0.1 M glucose (RT)	1.1	0.7	0.30	11
		0.5 M NaOH + 0.3 M glucose (RT)	0.90	2.02	0.30	
Pt (*unknown*)	PdBi/C (0.35 mg cm^{-2})	0.5 M NaOH + 0.5 M glucose (RT)	0.95	1.5	0.3	12
Pt@carbon paper (0.35 mg cm^{-2})	Au@carbon paper (0.35 mg cm^{-2})	0.5 M NaOH + 0.3 M glucose (RT)	1.02	1.7 ± 0.1	0.40	Here
	Pt@carbon paper (0.35 mg cm^{-2})[b]		0.99	1.8 ± 0.1	0.73	
	Pt@carbon paper (0.35 mg cm^{-2})[c]		1.00	3.1 ± 0.1	0.67	

[a] Operated in flow cell (as those gathered by Santiago et al.[13]) by supplying continuously 0.5 M D-glucose solution dissolved in distilled water or 0.5 M KOH to the anode at 4 mL min^{-1}, and humidified oxygen to the cathode at 100 mL min^{-1}. And it used very high noble metal loading of 3 mg/cm^2 that is over the recommended loading (should be lower than 0.4 mg/cm^2 in electrocatalysts).

[b] Used surface: 1 cm^2

[b]Used surface: 2 cm^2

Fig. S1 displays SEM images of the used support showing different fibers (filled tubes) with a diameter of ca. 8 µm, a porosity of 20-50 µm and 190 µm as thickness, i.e., composed of ca. 23 fiber layers.

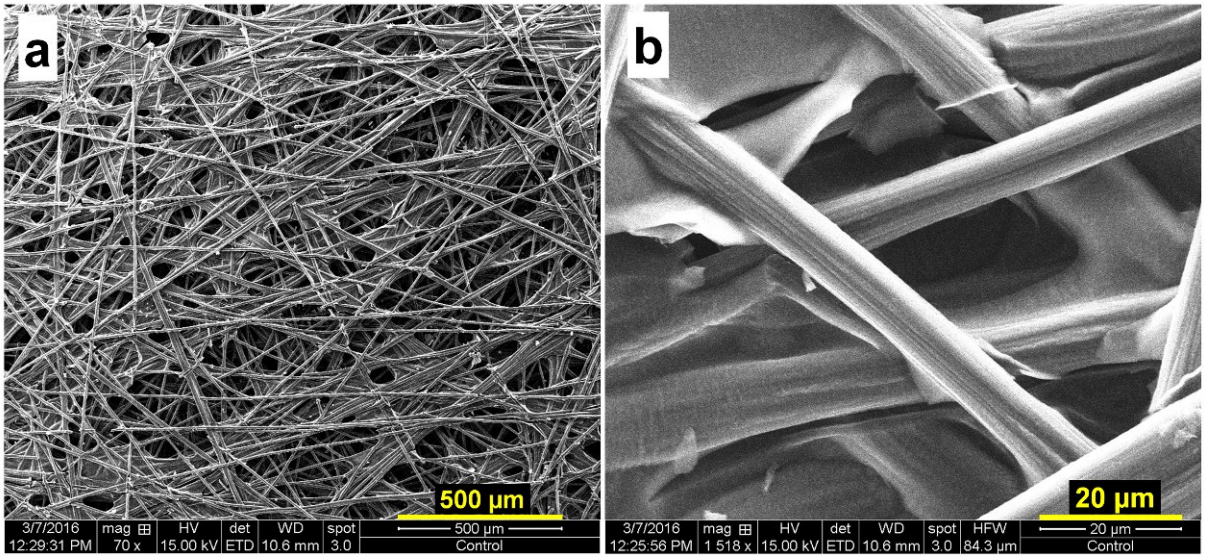

Fig. S1 As-received Toray carbon paper TGP-060-H: (a) SEM and (b) HRSEM micrographs.

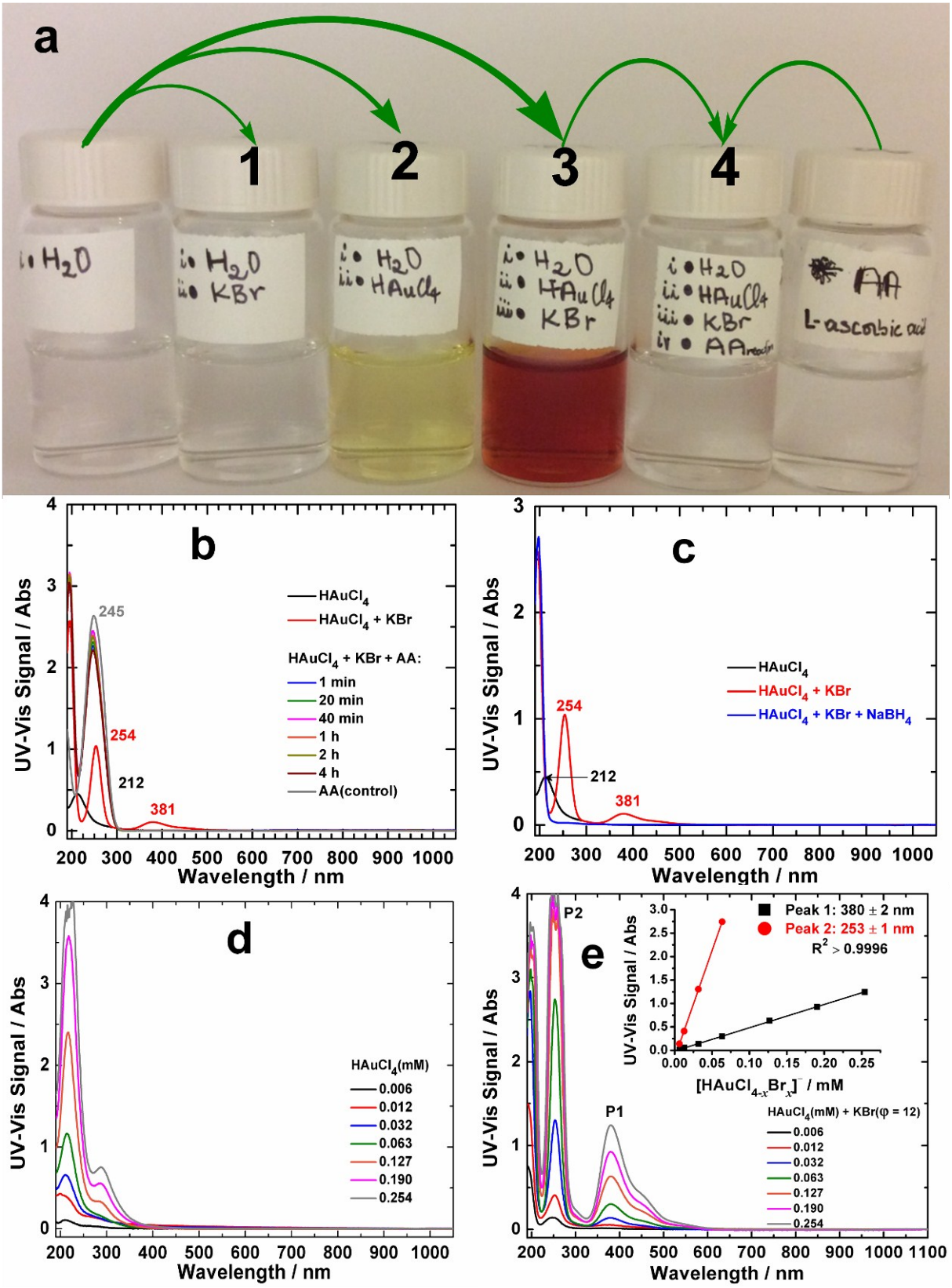

Fig. S2 (a) Photo of the samples showing the colour change upon the addition of KBr (as can be seen in (e) by the presence of a strong absorption, Peak 1) or L-ascorbic acid (AA). (b, c) UV-Vis spectra recorded during the synthesis using (b) AA or (c) $NaBH_4$ as reduction agents: 50 µL of the indicated concentrated is diluted with 3950 µL of H_2O (80-time) before measurement in a quartz cuvette of 1 cm path. (d, e) UV-Vis spectra of the aqueous solutions of $HAuCl_4$ in the absence and presence of KBr for $\varphi = n(KBr)/n(HAuCl_4) = 12$: 20 µL of the indicated concentrated is diluted with 1980 µL of H_2O (100-time) before measurement in a quartz cuvette of 1 cm path.

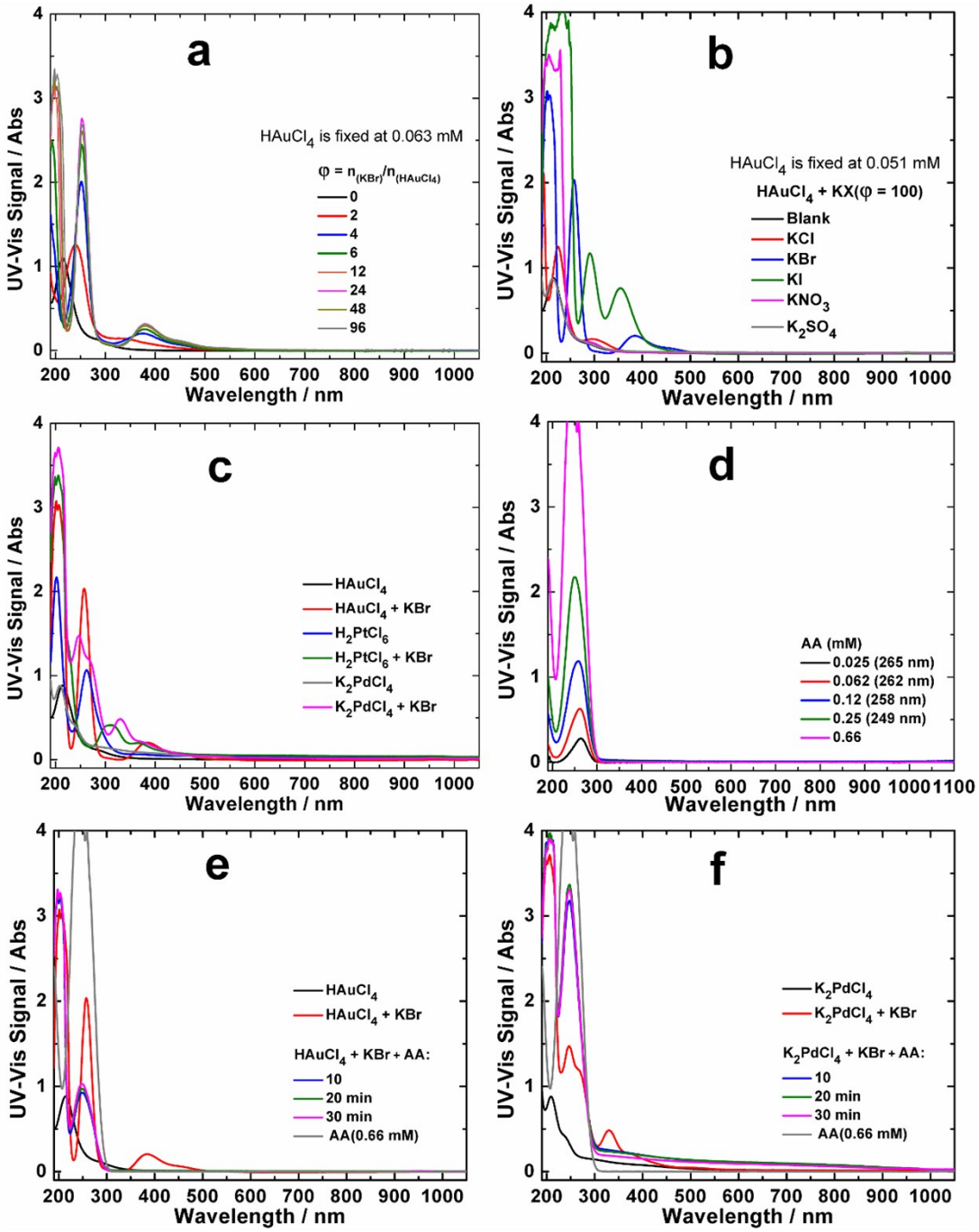

Fig. S3 (a) UV-Vis spectra of $HAuCl_4$ aqueous solution in presence of different amount of KBr. (b) UV-Vis spectra recorded upon the addition of different halides, nitrate and sulphate to "mediate" the gold particles growth process during the synthesis. (c) UV-Vis spectra of the aqueous solutions of $HAuCl_4$, H_2PtCl_6 and K_2PdCl_4 and the effect of KBr, as described in the experimental section. (d) UV-Vis spectra of L-ascorbic acid (AA) at different concentration. (e, f) Comparative UV-Vis spectra during the synthesis of Au and Pd materials as described in the experimental section.

Note: For (a-f), 20 µL of the indicated sample is diluted with 1980 µL of H_2O (100-time) before measurement in a quartz cuvette of 1 cm path. Upon the addition of KBr, UV-Vis spectra (Fig. S3c) show that the pristine complexes $[PdCl_4]^{2-}$ (peaks at 208 and 240 nm) and $[PtCl_6]^{2-}$ (peaks at 202 and 262 nm) have been replaced by those of $[PdBr_4]^{2-}$ (peaks at 246, 273 and 329 nm) and $[PtBr_6]^{2-}$ (peaks at 310 and 370 nm).

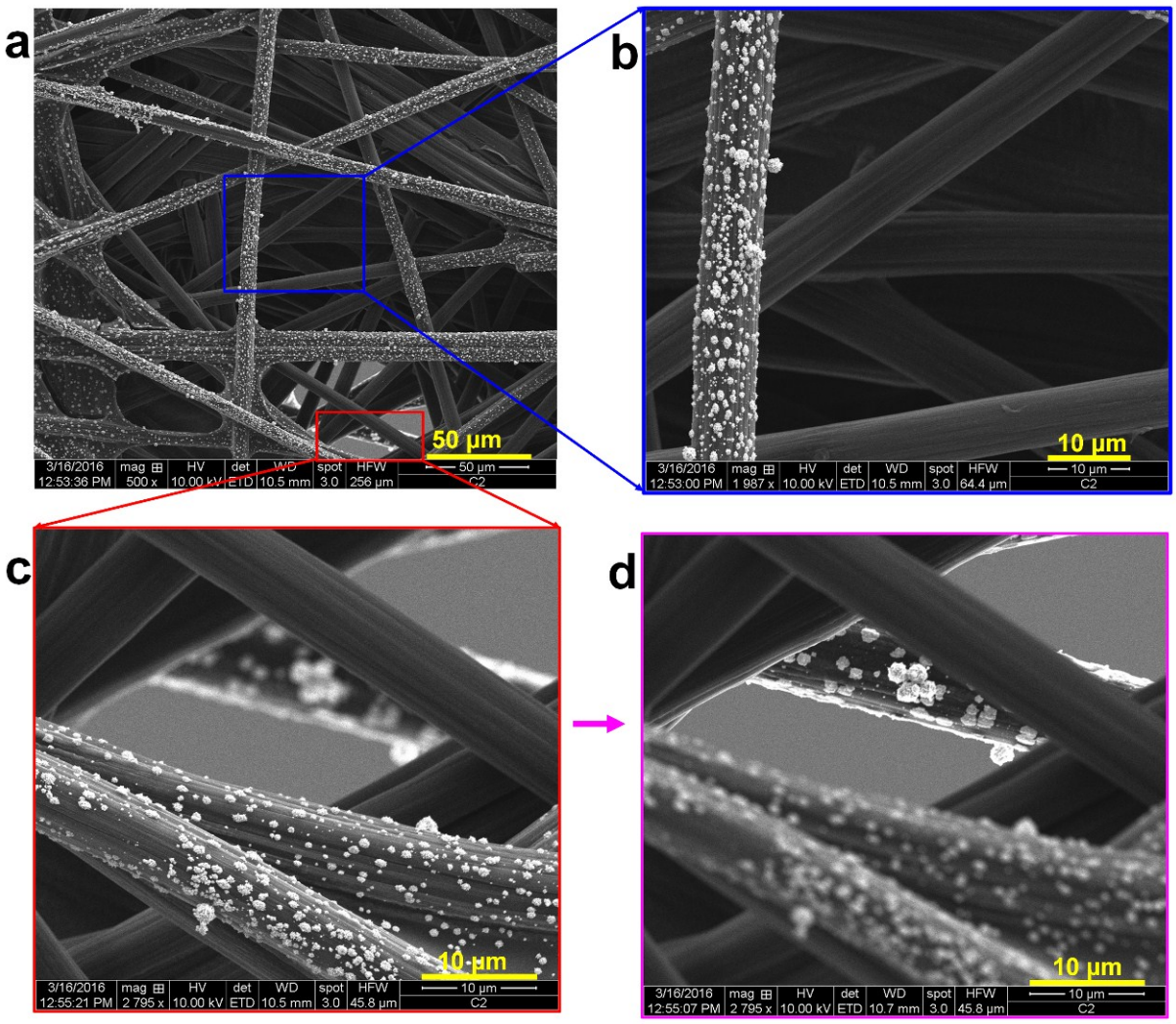

Fig. S4 Structural and morphological characterizations of gold particles growth on Toray carbon paper (in the presence of Br^-) for $n(KBr)/n(HAuCl_4)$ = 12 and 4 wt.% Au (i.e. 0.2 mg_{metal} cm^{-2}) at room temperature for the reaction time of 30 min. (a-c) Front and (d) Back views SEM micrographs with different magnifications showing that only the first 1-2 layers of fibers are decorated by gold.

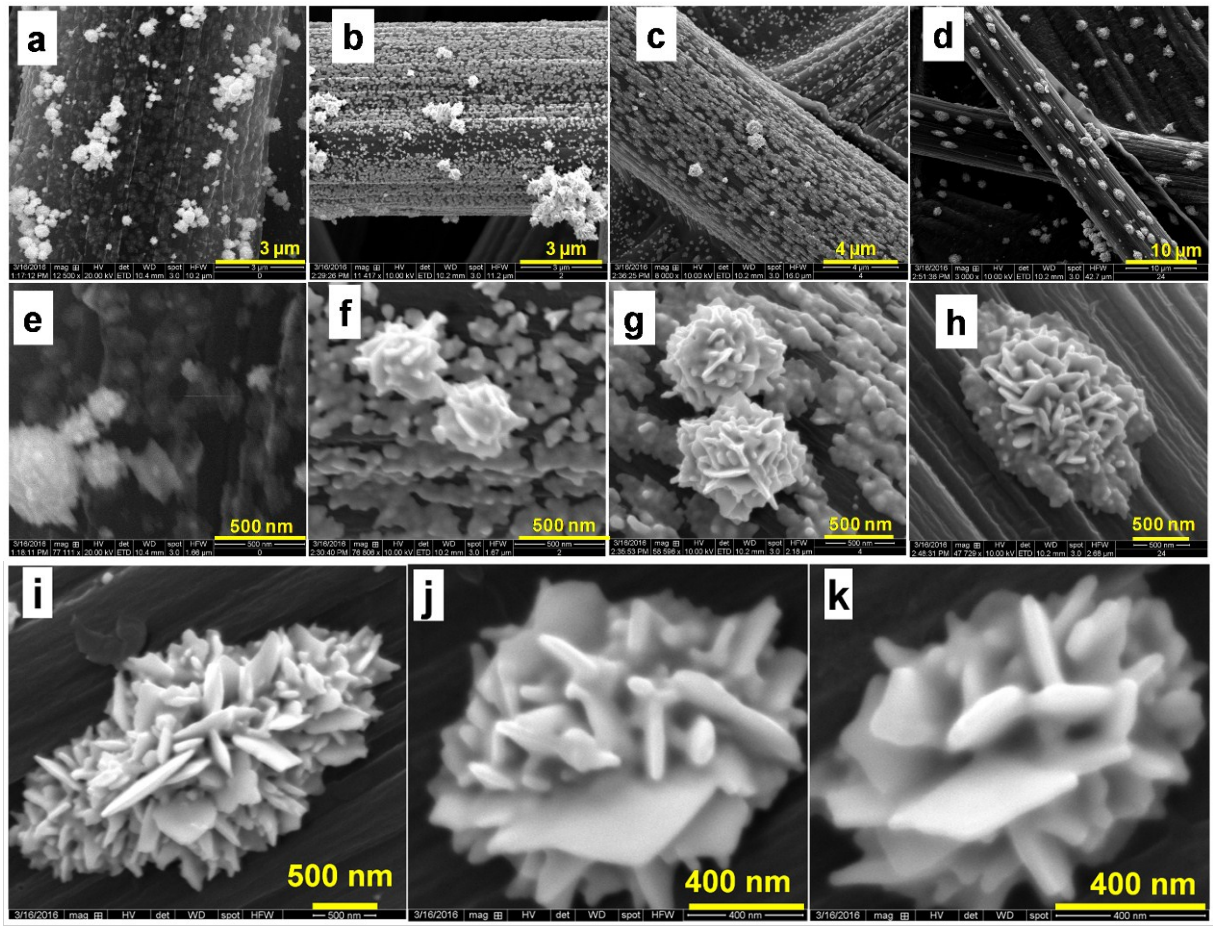

Fig. S5 Structural and morphological characterizations of gold particles growth on Toray carbon paper (in the presence of Br^-) for different amount of KBr and at room temperature for the reaction time of 30 min. SEM micrographs with different magnifications: (a, e) n(KBr)/n($HAuCl_4$) = 0; (b, f) n(KBr)/n($HAuCl_4$) = 2; (c, g) n(KBr)/n($HAuCl_4$) = 4; (d, h) n(KBr)/n($HAuCl_4$) = 24 and (i-k) n(KBr)/n($HAuCl_4$) = 96.

Note: For the studies of n(KBr)/n($HAuCl_4$) ratios from 0-96, only KBr amount was varied and that of gold salt was kept constant towards the targeted metal loading of 4 wt.% Au (i.e. 0.2 mg_{metal} cm^{-2}).

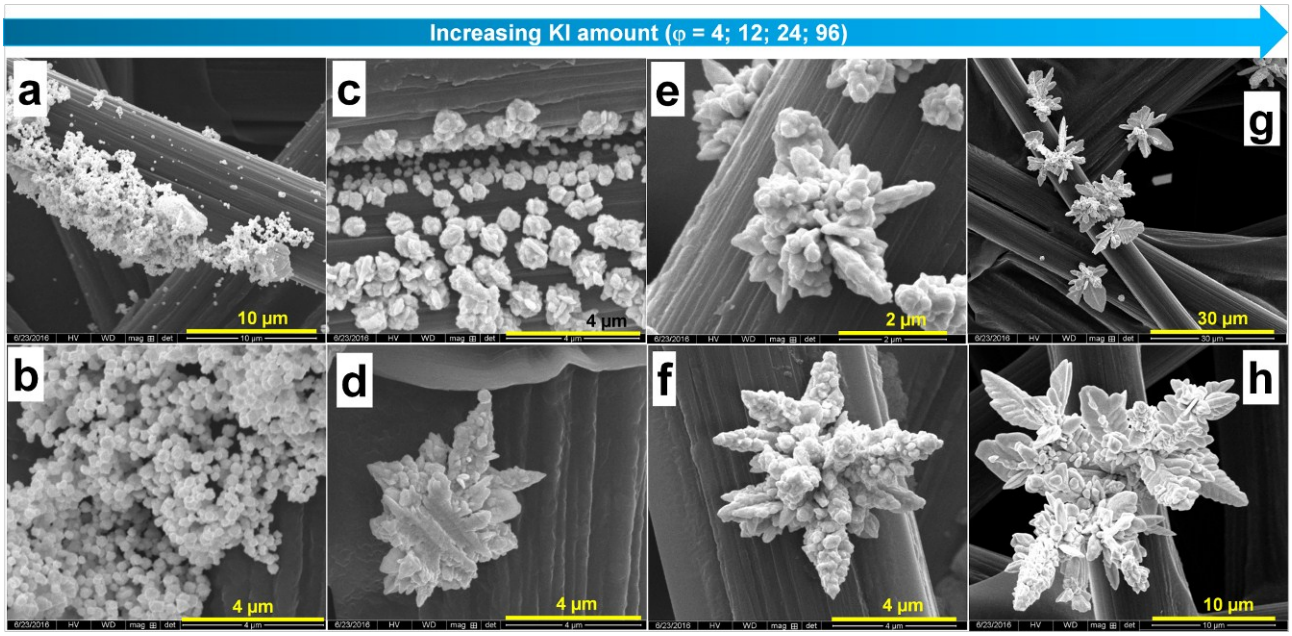

Fig. S6 Structural and morphological characterizations of gold particles growth on Toray carbon paper (in the presence of I^-) for different amount of KI and at room temperature for the reaction time of 30 min. SEM micrographs with different magnifications: (a, c) n(KI)/n($HAuCl_4$) = 4, (c, d) n(KI)/n($HAuCl_4$) = 12, (e, f) n(KI)/n($HAuCl_4$) = 24 and (g, h) n(KI)/n($HAuCl_4$) = 96.

Note: For the studies of n(KI)/n($HAuCl_4$) ratios from 0-96, only KBr amount was varied and that of gold salt was kept constant towards the targeted metal loading of 4 wt.% Au (i.e. 0.2 mg_{metal} cm^{-2}).

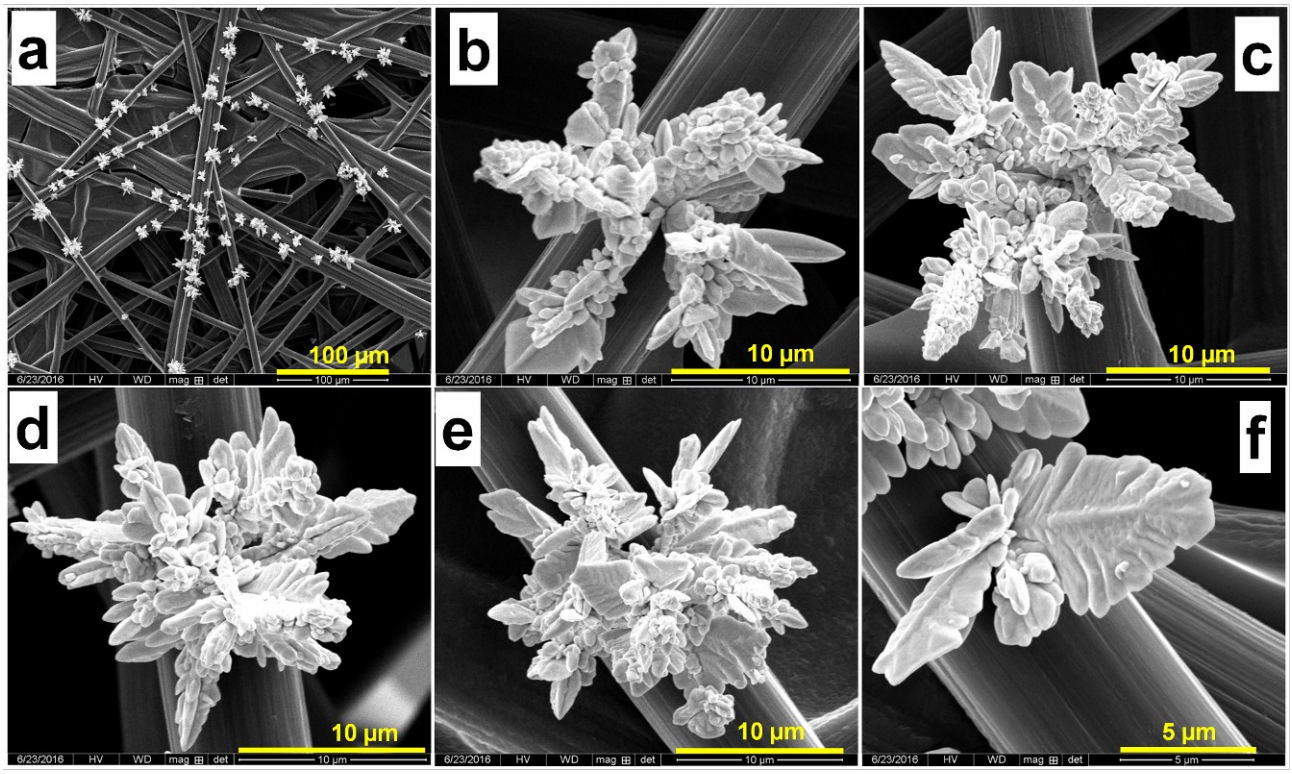

Fig. S7 Structural and morphological characterizations of gold particles growth on Toray carbon paper (in the presence of I^-) for different amount of KI and at room temperature for the reaction time of 30 min. (a-c) SEM micrographs with different magnifications for n(KI)/n($HAuCl_4$) = 96 showing the detailed view of nanothorn assemblies.

Note: Targeted metal loading of 4 wt.% Au (i.e. 0.2 mg_{metal} cm^{-2}).

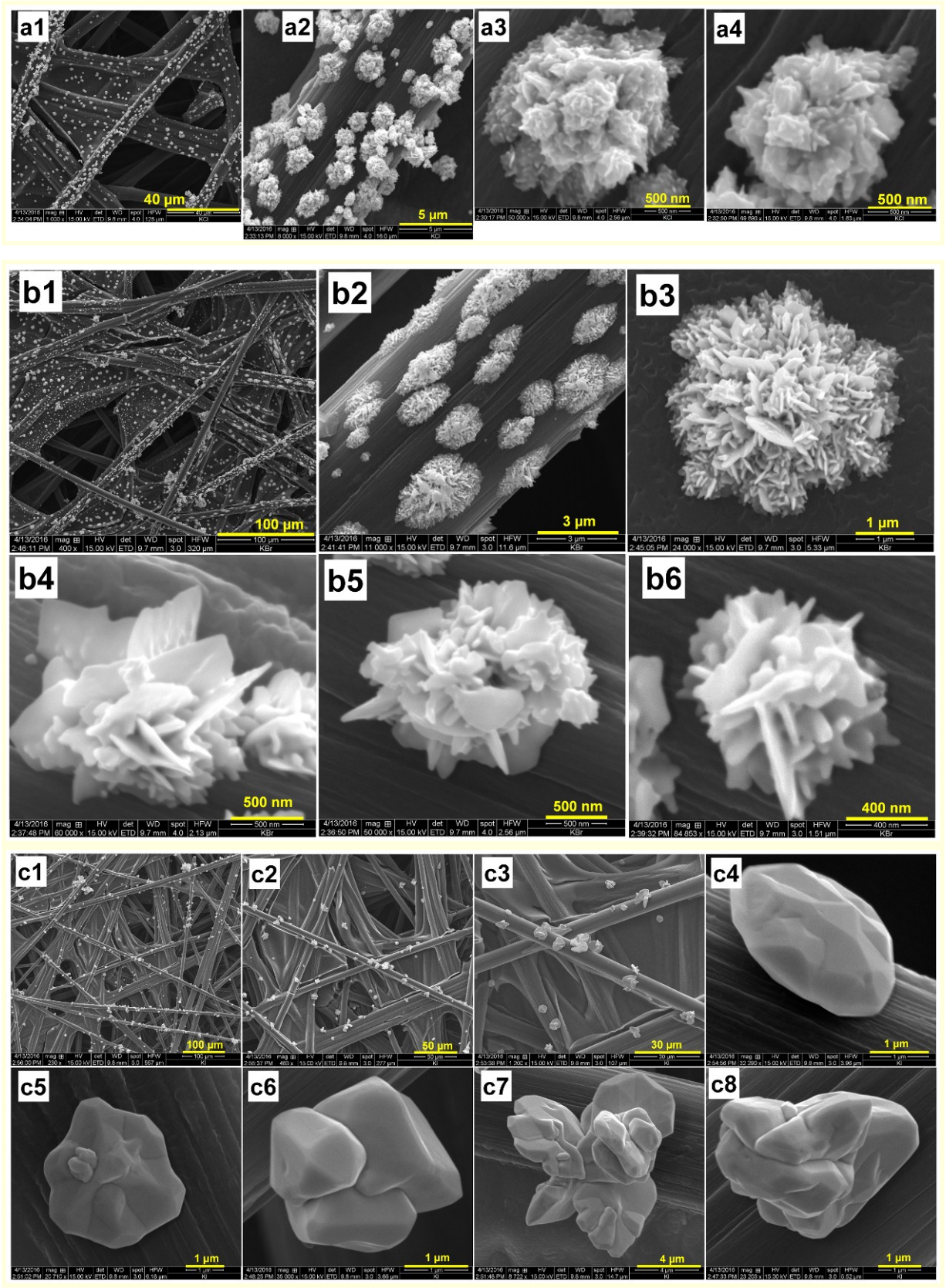

Fig. S8 Morphological characterization of anisotropic gold particles growth on Toray carbon paper (in the presence of halide ions) for $n(\mathbf{KX})/n(HAuCl_4) = 100$ and 8 wt.% Au (i.e. 0.4 mg_{metal} cm^{-2}) at room temperature for the reaction time of 30 min. SEM/HRSEM micrographs with different magnifications: (a1-a4) $\boldsymbol{X} = Cl^-$, (b1-b6) $X = Br^-$ and (c1-c8) $\boldsymbol{X} = I^-$.

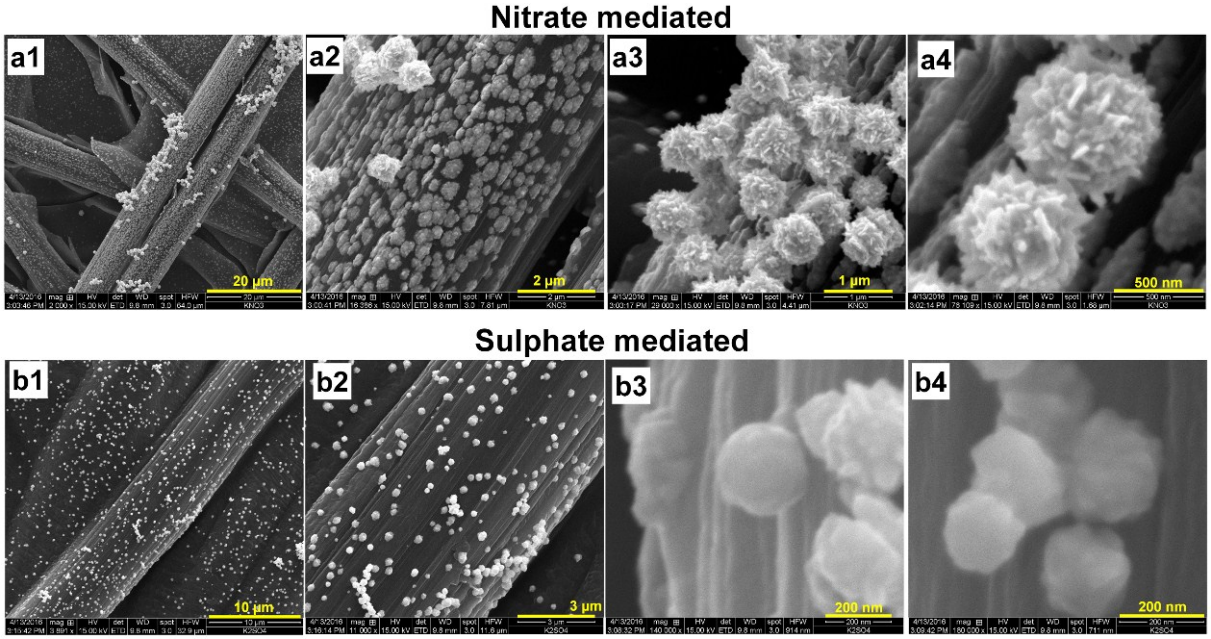

Fig. S9 Morphological characterization of anisotropic gold particles growth on Toray carbon paper (in the presence of nitrate and sulphate) for 8 wt.% Au (i.e. 0.4 mg_{metal} cm^{-2}) at room temperature for the reaction time of 30 min. SEM/HRSEM micrographs with different magnifications: (a1-a4) NO_3^- for $n(KNO_3)/n(HAuCl_4) = 100$ and (b1-b4) SO_4^{2-} for $n(K_2SO_4)/n(HAuCl_4) = 100$.

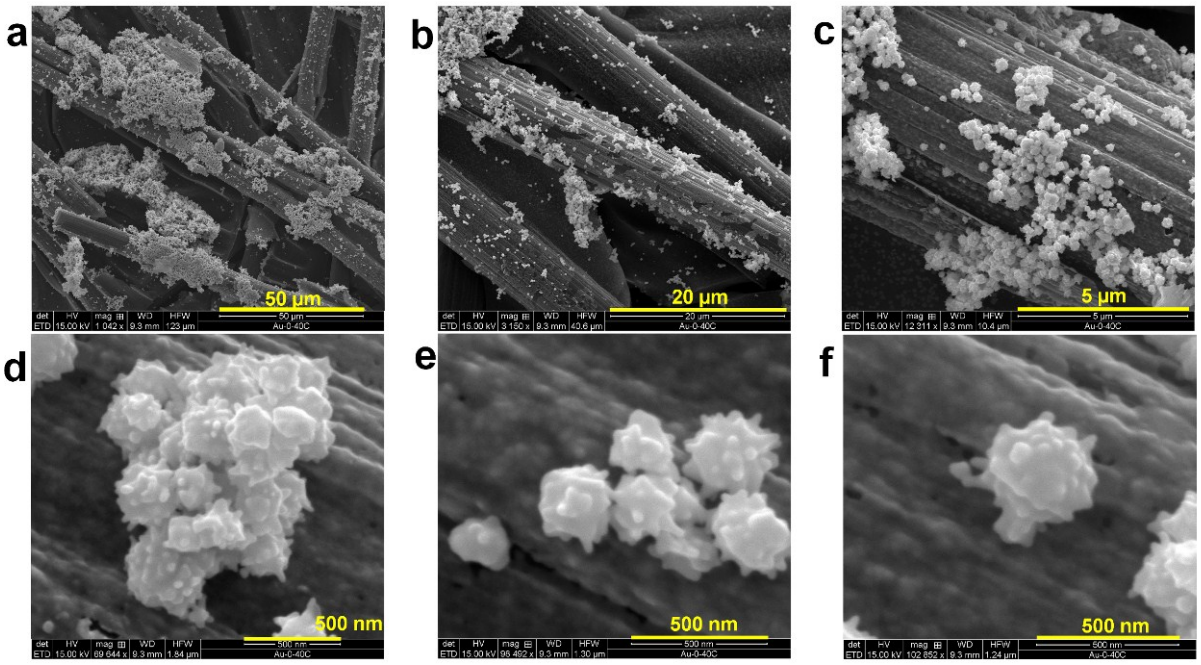

Fig. S10 Morphological characterizations of gold particles growth on Toray carbon paper at 40 °C for the reaction time of 30 min. SEM/HRTEM micrographs with different magnifications of the control synthesis in the absence of halide at 40 °C. Note the targeted metal loading was 8 wt.% Au (i.e. 0.4 mg_{metal} cm^{-2}).

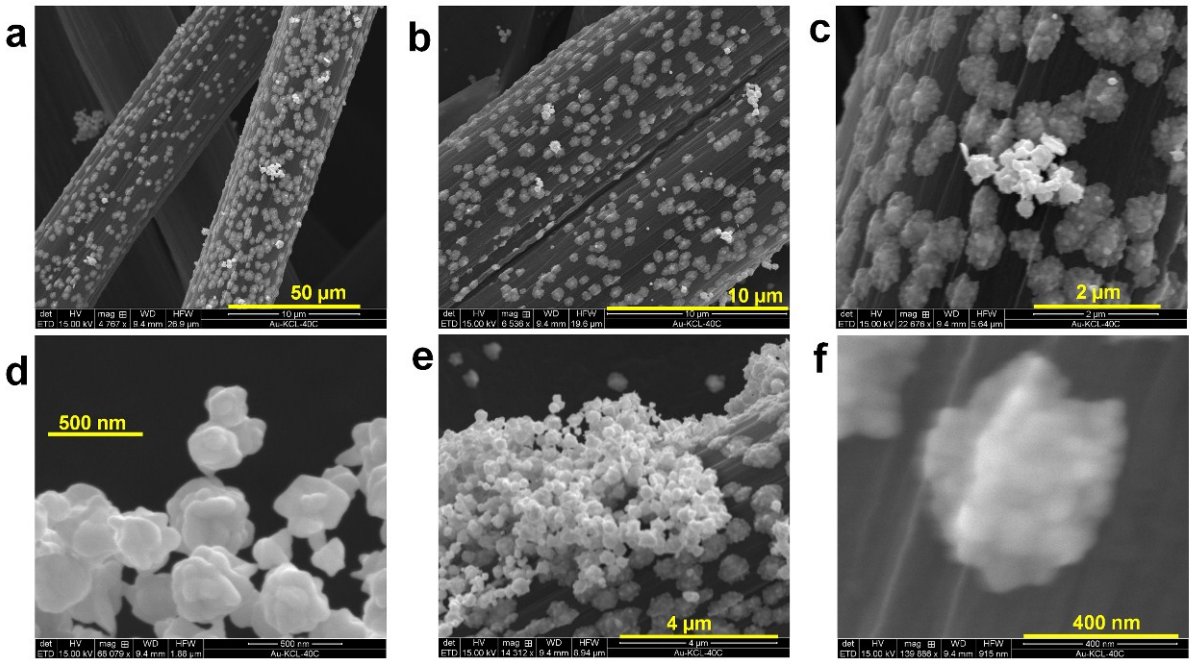

Fig. S11 Morphological characterizations of gold particles growth on Toray carbon paper at 40 °C for the reaction time of 30 min. SEM/HRTEM micrographs with different magnifications of the control synthesis in the presence of Cl^- for n(KCl)/n($HAuCl_4$) = 100 at 40 °C. Note the targeted metal loading was 8 wt.% Au (i.e. 0.4 mg_{metal} cm^{-2}).

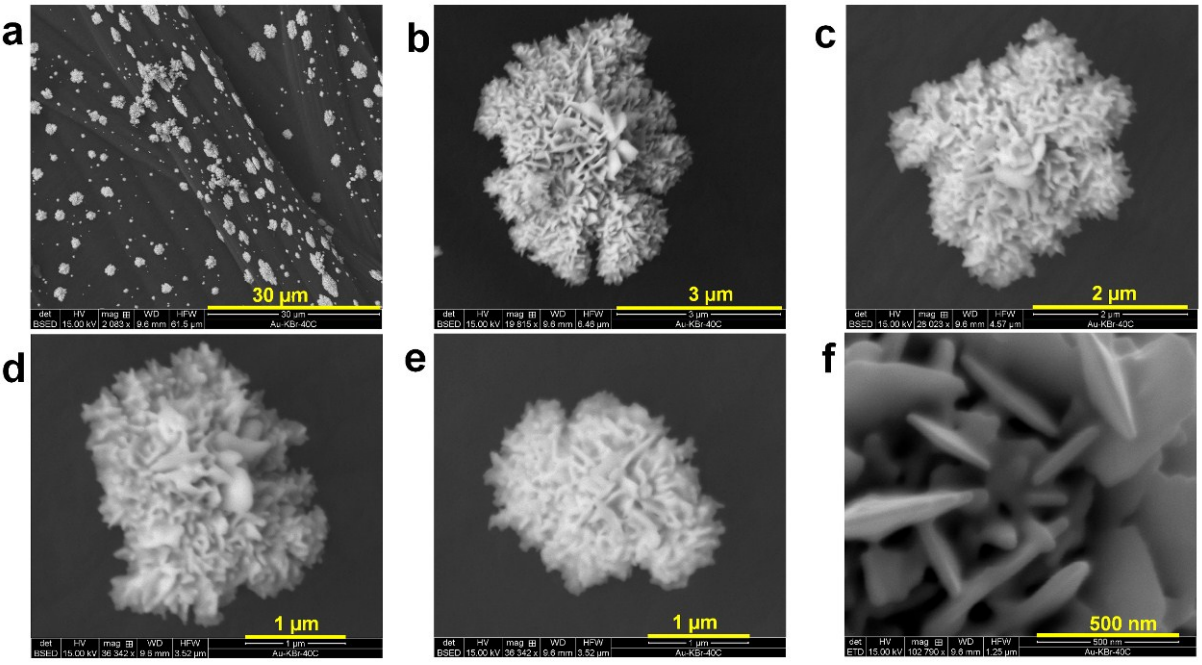

Fig. S12 Morphological characterizations of gold particles growth on Toray carbon paper at 40 °C for the reaction time of 30 min. SEM/HRTEM micrographs with different magnifications of the control synthesis in the presence of Br^- for n(KBr)/n($HAuCl_4$) = 100 at 40 °C. Note the targeted metal loading was 8 wt.% Au (i.e. 0.4 mg_{metal} cm^{-2}).

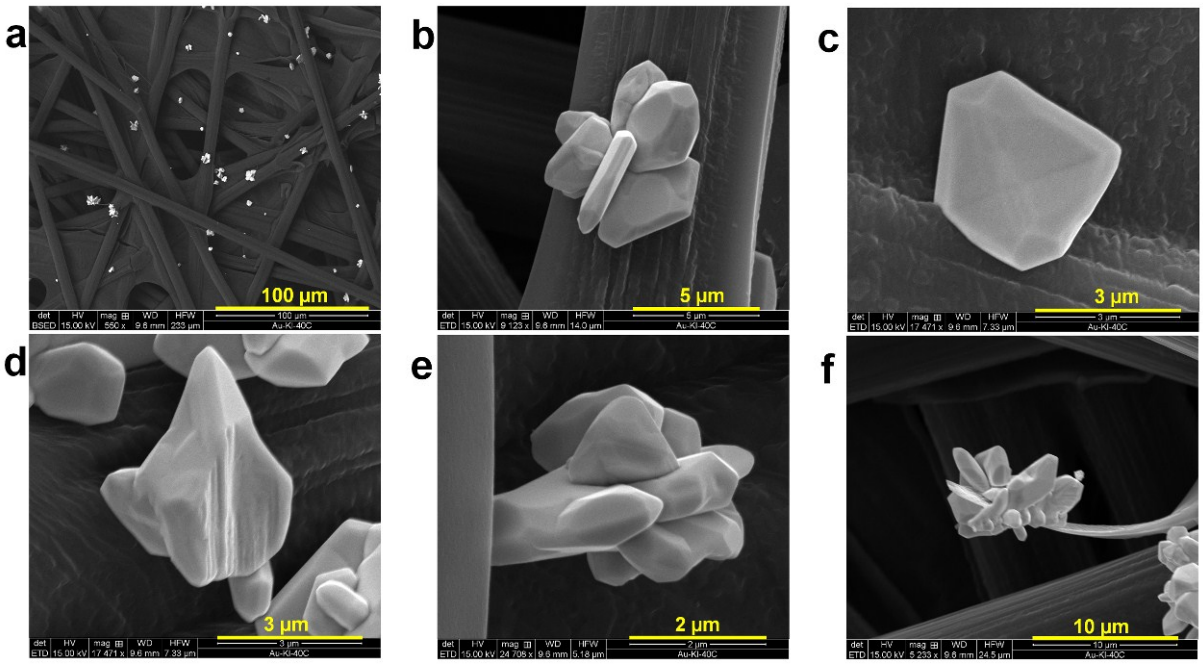

Fig. S13 Morphological characterizations of gold particles growth on Toray carbon paper at 40 °C for the reaction time of 30 min. SEM/HRTEM micrographs with different magnifications of the control synthesis in the presence of I^- for n(KI)/n($HAuCl_4$) = 100 at 40 °C.

Note the targeted metal loading was 8 wt.% Au (i.e. 0.4 mg_{metal} cm^{-2}).

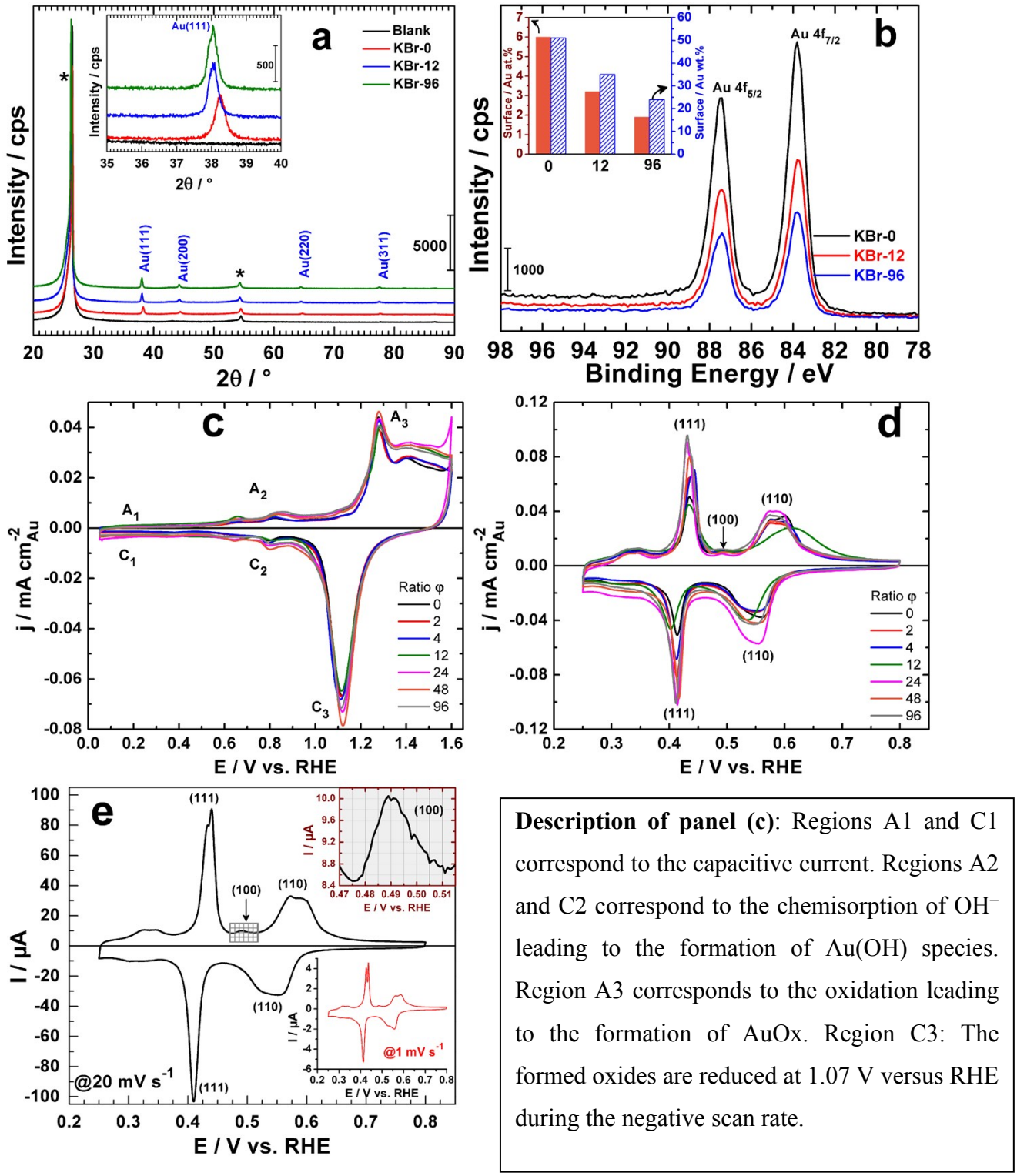

Description of panel (c): Regions A1 and C1 correspond to the capacitive current. Regions A2 and C2 correspond to the chemisorption of OH^- leading to the formation of Au(OH) species. Region A3 corresponds to the oxidation leading to the formation of AuOx. Region C3: The formed oxides are reduced at 1.07 V versus RHE during the negative scan rate.

Fig. S14 (a-d) Physicochemical and electrochemical characterizations of gold particles growth on Toray carbon paper (in the presence of Br^-) TGH-H-060 (4 wt.%, i.e. 0.2 mg_{metal} cm^{-2}) for different ratios of φ = n(KBr)/n($HAuCl_4$) also labelled as "KBr-x": (a) XRD patterns, inset shows the patterns for Au (111) crystallographic plane; (b) High-resolution XPS spectra of the Au 4f core level, inset shows the surface atomic (at.%: left y-axis) and weight (wt.%, right y-axis) composition of Au; (c) CVs recorded in 0.1 M NaOH at 20 mV s^{-1} and (d) UPD of lead of in 0.1 M NaOH and 1 mM $Pb(NO_3)_2$ at 20 mV s^{-1}. (e) UPD of lead of in 0.1 M NaOH and 1 mM $Pb(NO_3)_2$ at 20 mV s^{-1} for Toray carbon paper TGH-H-060, 8 wt.% Au (i.e. 0.4 mg_{metal} cm^{-2}) and φ = 100.

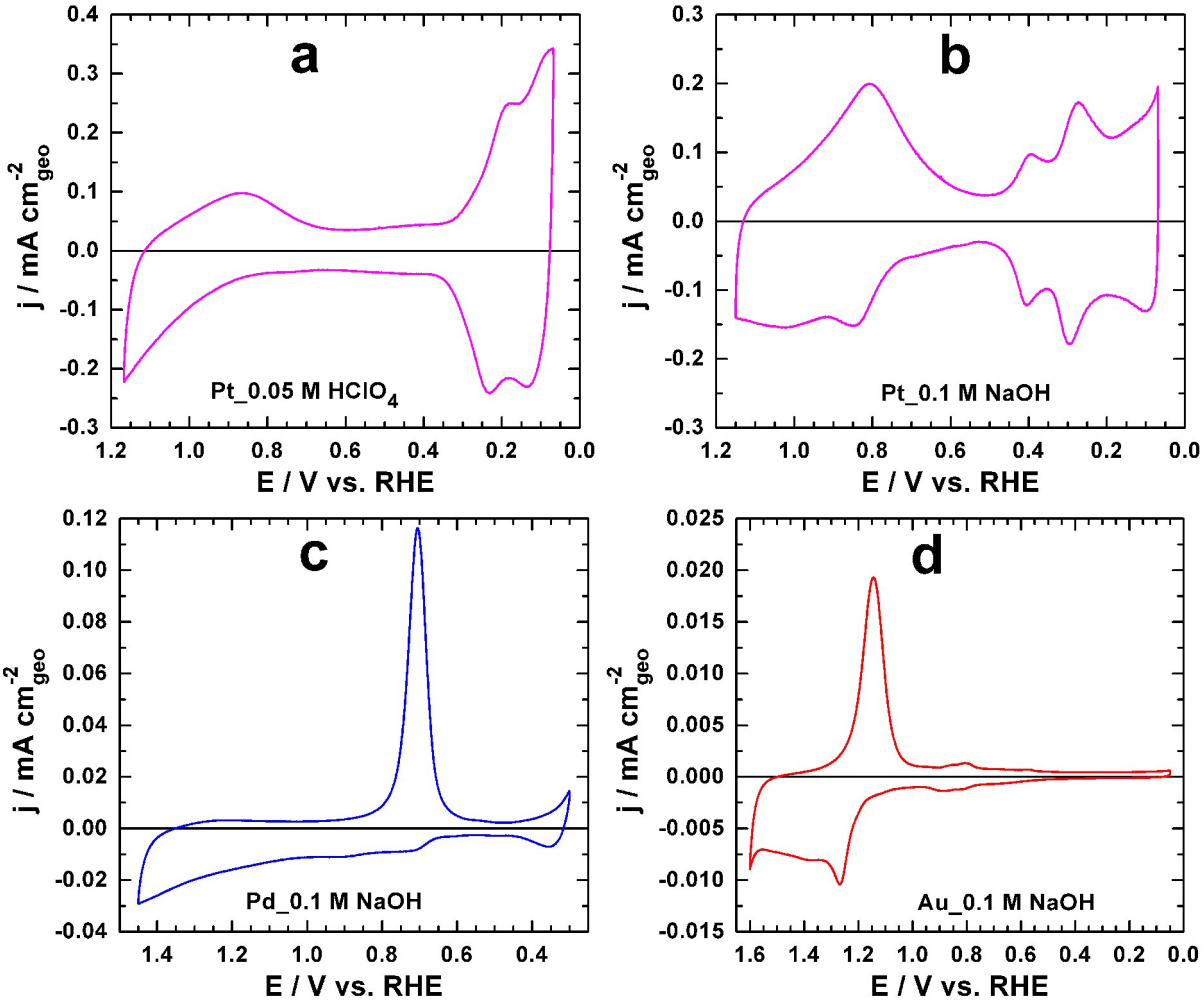

Fig. S15. Electrochemical characterizations of the as-synthesized metals on Toray carbon TGH-H-060 at 40 °C for the metal loading of 8 wt.% (i.e. 0.4 mg_{metal} cm^{-2}). Comparative steady-state cyclic voltammograms recorded under N_2-saturated electrolyte at 5 mV s^{-1} scan rate for: (a) Pt in 0.05 M $HClO_4$, (b) Pt in 0.1 M NaOH, (c) Pd in 0.1 M NaOH and (d) CV of Au in 0.1 M NaOH.

Note: **Panels (a-b)** The hydrogen desorption from Pt sites occurs during the positive potential-going scan between 0.05 and 0.4 V vs. RHE, followed by the double layer charging current up to 0.7 V vs. RHE and finally the Pt surface oxidation at higher potentials. In the reverse scan, the Pt oxide reduction corresponding to the cathodic peak takes place at 0.7 V vs. RHE. Then, the Pt free surface becomes covered by adsorbed hydrogen in the lower potential region (from 0.4 to 0.05 V vs. RHE). **Panel (c)** The positive scan is characterized by the adsorption of hydroxyl species onto Pd surface about 0.7 V vs. RHE follows by the first PdO monolayer formation; which ends at 1.45 V vs. RHE. The cathodic variation of the potential shows a main PdO reduction peak, centered at 0.7 V vs. RHE depending on the particles size, the value of the upper potential limit and the scan rate.

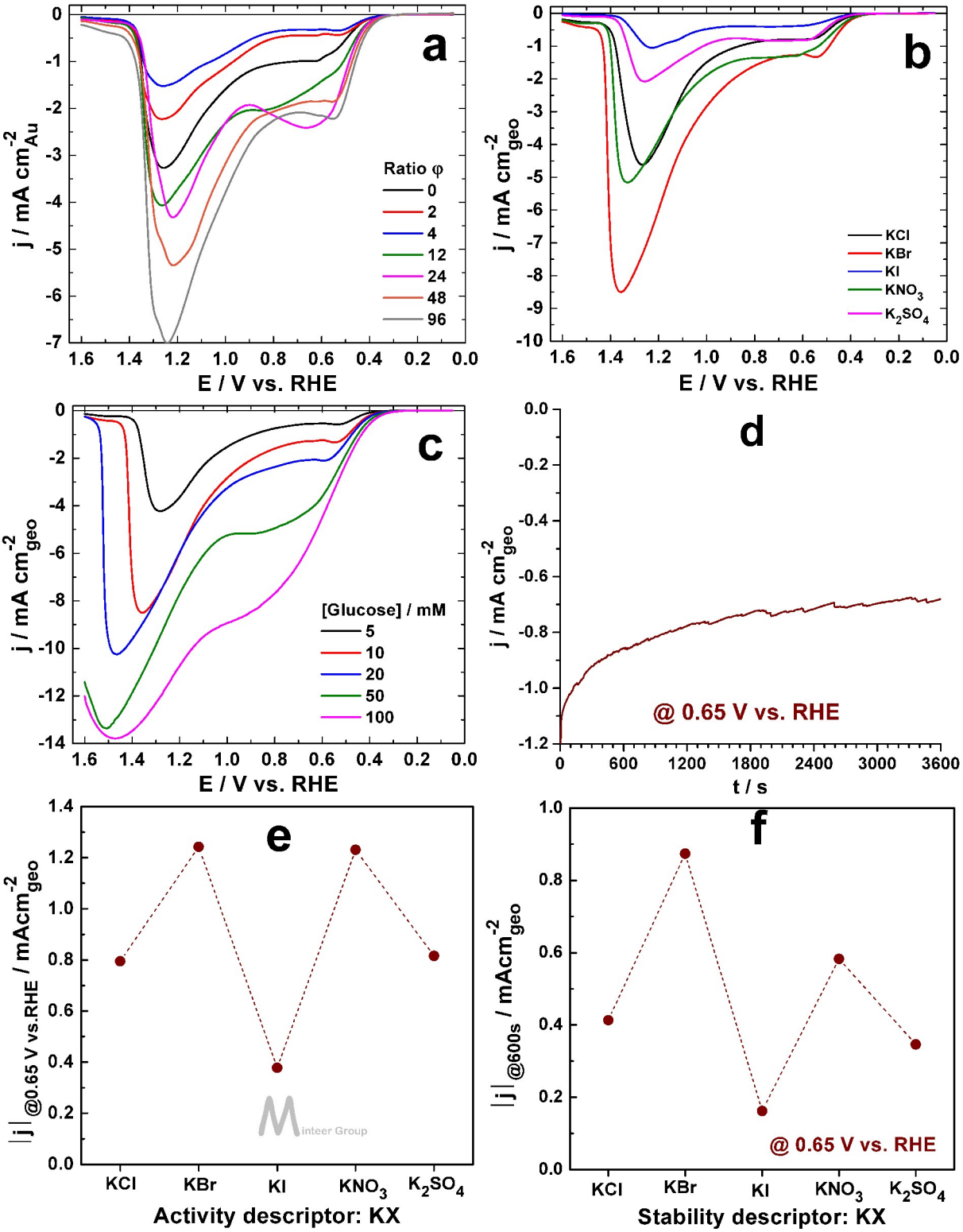

Fig. S16 Electrocatalytic properties of the synthesized Au materials (growth on Toray carbon paper) towards glucose (10 mM) electrooxidation in 0.1 M NaOH. (a) Effect of φ = n(KBr)/n($HAuCl_4$) ratios for Br^- (4 wt.% Au, i.e. 0.2 mg_{metal} cm^{-2}): Voltammograms recorded at 20 mV s^{-1}. (b) Effect of halides, nitrate and sulphate mediated for n(KX)/n($HAuCl_4$) = 100 at 8 wt.% Au (i.e. 0.4 mg_{metal} cm^{-2}): Voltammograms recorded at 50 mV s^{-1}. (c) Glucose concentration effect for φ = n(KBr)/n($HAuCl_4$) = 100 (8 wt.% Au, i.e. 0.4 mg_{metal} cm^{-2}): Voltammograms recorded at 50 mV s^{-1}. (d) Chronoamperometry recorded at 0.65 V vs. RHE for n(KBr)/n($HAuCl_4$) = 100 (8 wt.% Au, i.e. 0.4 mg_{metal} cm^{-2}). (e, f) Performances descriptors from (b) and chronoamperometry for n(KBr)/n($HAuCl_4$) = 100 (8 wt.% Au, i.e. 0.4 mg_{metal} cm^{-2}).

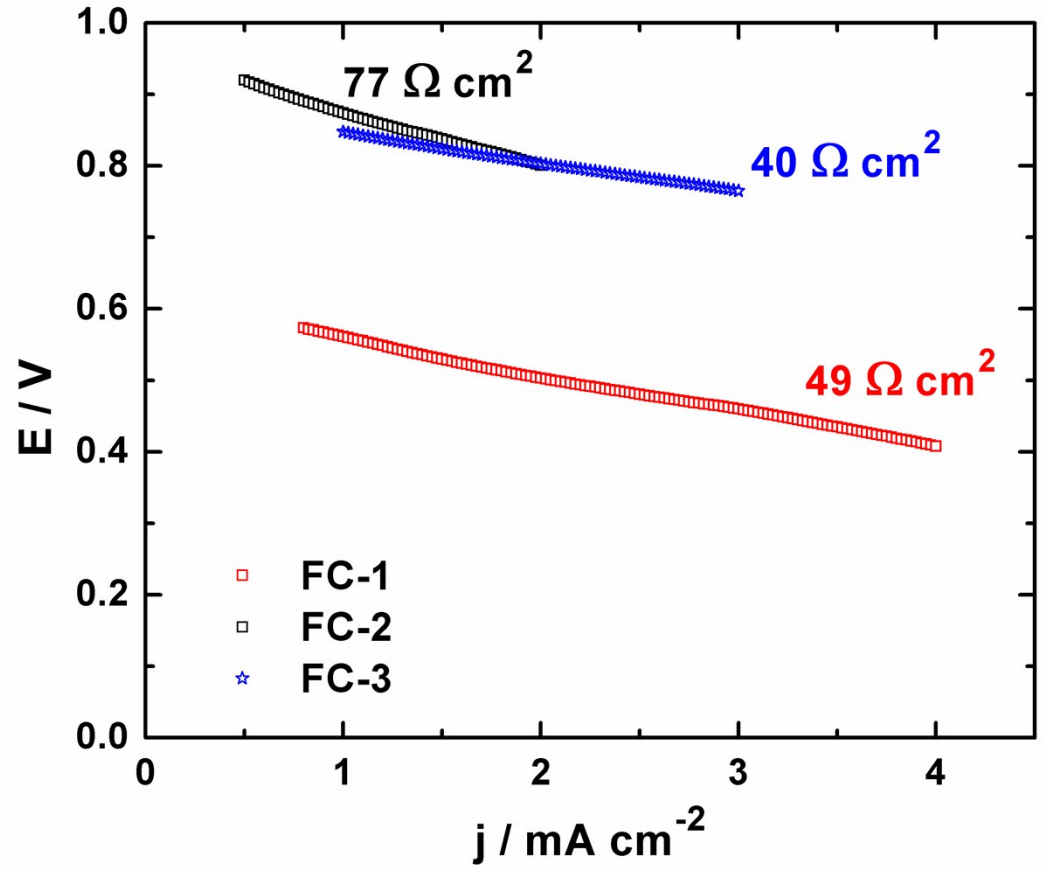

Fig. S17 Electrochemical characterization of the as-synthesized materials for the metal loading of 8 wt.% (i.e. 0.4 mg_{metal} cm^{-2}). Fuel cell polarization curves (iR-uncorrected) for the determination of the ohmic resistance: The Pt cathode (1 cm^2) operated in 0.5 M NaOH + O_2; the Au anode (1 cm^2 for FC-1), Pt anode (1 cm^2 for FC-2) and Pt anode (2 cm^2 for FC-3) operated in 0.5 M NaOH + 0.3 M glucose; a Fumatech AEM separated both compartments.

Note: FC-1 and FC-2: Anode and Cathode are pressed against AEM; FC-3 only the cathode is pressed against the AEM and the anode is situated close to AEM (about 1-2 cm).

References

1. A. Usher, D. C. McPhail and J. Brugger, *Geochim. Cosmochim. Acta*, 2009, **73**, 3359-3380.
2. J. J. Lingane, *J. Electroanal. Chem.*, 1962, **4**, 332-342.
3. D. H. Evans and J. J. Lingane, *J. Electroanal. Chem.*, 1963, **6**, 1-10.
4. D. Basu and S. Basu, *Electrochim. Acta*, 2010, **55**, 5775-5779.
5. L. Li, K. Scott and E. H. Yu, *J. Power Sources*, 2013, **221**, 1-5.
6. D. Basu and S. Basu, *Int. J. Hydrogen Energy*, 2012, **37**, 4678-4684.
7. D. Basu and S. Basu, *Electrochim. Acta*, 2011, **56**, 6106-6113.
8. S.-P. Tung, T.-K. Huang, C.-Y. Lee and H.-T. Chiu, *RSC Adv.*, 2012, **2**, 1068-1073.
9. D. Orton and D. Scott, *J. Power Sources*, 2015, **295**, 92-98.
10. N. Fujiwara, S.-i. Yamazaki, Z. Siroma, T. Ioroi, H. Senoh and K. Yasuda, *Electrochem. Commun.*, 2009, **11**, 390-392.
11. Y. Holade, K. Servat, T. W. Napporn, C. Morais, J.-M. Berjeaud and K. B. Kokoh, *ChemSusChem*, 2016, **9**, 252-263.
12. C.-C. Chen, C.-L. Lin and L.-C. Chen, *J. Power Sources*, 2015, **287**, 323-333.
13. Ó. Santiago, E. Navarro, M. A. Raso and T. J. Leo, *Appl.Energy*, 2016, **179**, 497-522.